DTU candidate field models for IGRF-13

C.C. Finlay, C. Kloss, N. Olsen, M. Hammer and L. Tøffner-Clausen
DTU Space, Technical University of Denmark

Draft, October 1, 2019

1 Introduction

This note provides information on the construction of the DTU candidate models for IGRF-13: DGRF epoch 2015, IGRF epoch 2020 and predicted linear secular variation (SV) 2020-2025.

It describes the construction of the parent field model from which these were derived, CHAOS-7. This is the latest update of the CHAOS series of field models [Olsen et al., 2006, Olsen et al., 2014, Finlay et al., 2016].

2 Data

CHAOS-7 is based on satellite data from the Ørsted, CHAMP, SAC-C, Cryosat-2 and the three *Swarm* satellites, as well as monthly mean ground observatory secular variation data.

2.1 Satellite data

From the Ørsted mission we used vector data between March 1999 and December 2004 and scalar data (for quasi-dipole latitudes poleward of $\pm 55^\circ$ or if attitude data were not available) between March 1999 and June 2013, each with 1 minute sampling. Along-track scalar gradients were used based on differences of scalar data separated by 15 sec along track, with 1 minute sampling of these differences.

From the CHAMP mission we used vector data between August 2000 and September 2010 (converted to scalar data at quasi-dipole latitudes poleward of $\pm 55^\circ$) with 1 minute sampling, as well as vector and scalar along-track gradients, separated by 15 sec along track with 1 minute sampling of the gradients. Vector and vector gradient data were used only when two star cameras were available.

From the SAC-C mission, we used scalar data with 1 minute sampling between January 2001 and December 2004. No along track gradients were used.

From the Cryosat-2 mission we used uncalibrated vector data from August 2010 to December 2014, from magnetometer FGM1, after corrections for temperature effects, magnetorquer currents, and other spacecraft effects [Olsen et al.,

2019]. Data were averaged to 1 minute values using a robust linear fit in the magnetometer frame.

From the *Swarm* mission, we used the MAGX_LR_1B 1 Hz calibrated data product, baseline 0505/0506, with an initial 1 minute sampling from the three satellites, Alpha, Bravo and Charlie from November 2013 to the end of August 2019. In addition along-track gradients were estimated for each satellite based on differences between data 15 sec apart, and east-west gradients were estimated from the lower pair Alpha and Charlie, using the 1 Hz data on Charlie with geocentric latitude closest to that of Alpha data, sampled each minute, with the condition the time difference was less than 50 sec (typically it was around 10 seconds or less). Finally Swarm data were further downsampled by a factor of three to account for the fact there are three contributing satellites.

The following data selection criteria were applied to all data sets in an effort to focus on the internal field of interest for IGRF.

- $Kp \leq 2^0$ (3^0 for gradients) and RC-index [Olsen et al., 2014], changing at most by 2 nT/hr (3 nT/hr for gradients)
- Merging electric field at the magnetopause averaged over the previous 2 hrs, $E_m \leq 0.8$ mV/m
- IMF B_z at the magnetopause averaged over the previous 2 hrs is positive
- IMF B_y at the magnetopause averaged over the previous 2 hrs is less than + 3 nT in the quasi-dipole northern hemisphere i.e. $-\infty < B_y < 3$nT, while in the quasi-dipole southern hemisphere it is greater than -3nT $-3\text{nT} < B_y < \infty$ [Friis-Christensen et al., 2017]
- Only data from dark regions (sun at least 10° below horizon), except for Cryosat-2 where calibration parameters and Euler angles are co-estimated from vector data from both dark and sunlit regions
- Vector and vector gradients used only equatorward of ±55° quasi-dipole latitude

2.2 Ground observatory data

Annual differences of revised observatory monthly means [Olsen et al., 2014] for the time interval Jan 1997 to July 2019 were used to provide additional constraints on the secular variation. Revised monthly means were derived from the hourly mean values of 182 observatories (including 11 with site changes during the considered time interval) which were checked for trends, spikes and other errors [Macmillan and Olsen, 2013]. Monthly means were calculated by a robust method based on Huber weights [Huber, 2004], from all local times at all latitudes. We removed estimates of the ionospheric (plus induced) field as predicted by the CM4 model [Sabaka et al., 2004] and the large-scale

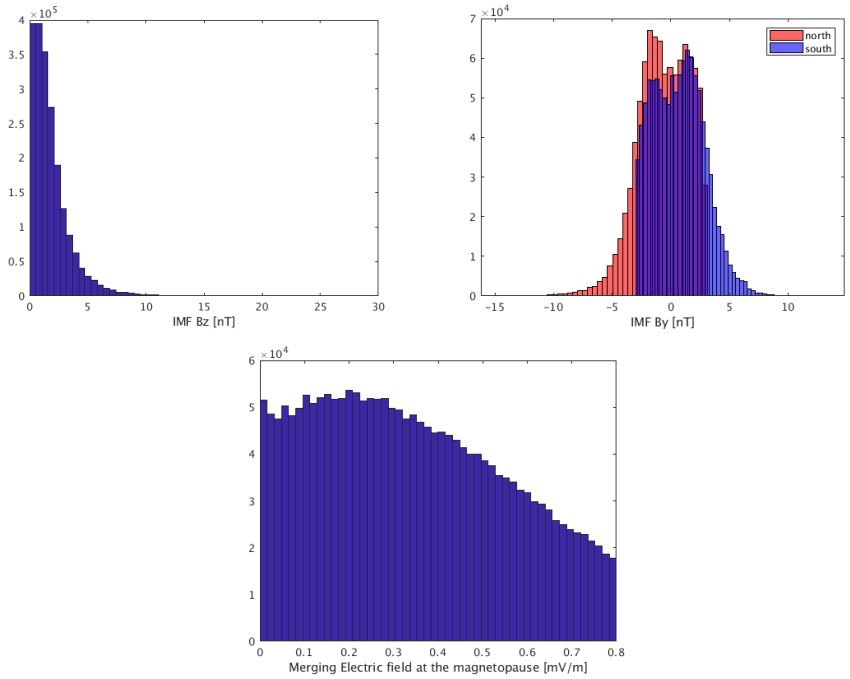

Figure 1: Histograms showing distribution of selected satellite data (combination of all the scalar, scalar gradient, vector and vector gradient data) according to IMF B_z (top left), IMF B_y (top right) and the Merging Electric field at the Magnetopause E_m, as estimated by coupling function $0.33v^{4/3}B_t^{2/3}\sin^{8/3}(|\Theta|/2)$ where , $B_t = \sqrt{B_y^2 + B_z^2}$ is the magnitude of the Interplanetary Magnetic Field in the $y-z$ plane in GSM coordinates and $\Theta = \arctan(B_y/B_z)$. IMF and Em values are averages of 1 minute values for 2 hours prior to the time of the observation. y-axis show the number of observations per bin.

magnetospheric (plus induced) field, predicted by a preliminary field model, CHAOS-6x9.

IAGA codes of observatories whose data were used are: AAA0, AAE1, ABG0, ABG1, ABK0, AIA0, ALE0, AMS0, AMT0 , API0 , API2, AQU0, ARS0, ASC0, ASP0, BDV0, BEL0, BFE0, BFO0, BGY1, BJN1, BLC0, BMT1, BNG0, BOU0, BOX0, BRW0, BSL0, BSL1, CBB0, CBI0, CDP0, CDP2, CKI0, CLF0, CMO3, CNB0, CNH3, COI0, CSY0, CSY1, CTA0, CTS0, CYG0, CZT0, DED0, DLR0, DLT0, DOB1, DOU0, DRV0, EBR0, ELT0, ESA0, ESK0, EYR0, FCC0, FRD0, FRN0, FUQ0, FUR0, GAN0, GCK0, GDH2, GLM0, GNA0, GNG0, GUA0, GUI0, GUI3, GZH2, HAD0, HBK0, HER0, HLP0, HON3, HRB0, HRN0, HTY0, HUA0, HYB0, IPM0, IQA0, IQA1, IRT2, IZN0, JAI0,

JCO0, KAK0, KDU0, KEP0, KHB0, KIR0, KIV2, KMH0, KMH1, KNY0, KNZ0, KOU0, KSH0, KSH1, LER0, LIV0, LMM0, LNP0, LON0, LOV0, LRM0, LRV0, LVV2, LYC0, LZH1, MAB0, MAW0, MBO0, MCQ0, MEA0, MGD0, MIZ0, MMB0, MNK0, MOS0, MZL0, NAQ0, NCK0, NEW0, NGK0, NGP1, NMP1, NUR0, NVS0, OTT0, PAF2, PAG0, PBQ0, PEG2, PET2, PHU0, PHU1, PIL0, PND0, PPT0, PST0, QGZ1, QIX0, QIX1, QSB0, QZH0, RES0, SBA0, SBL0, SFS2, SHL0, SHU0, SIL0, SIT2, SJG2, SOD3, SPT0, SSH0, STJ0, SUA0, SUA, TAM0, TAN0, TDC0, TEO0, TFS0, THJ0, THL0, THY0, TIR0, TIR1, TND0, TRO0 , TRW0, TSU0, TUC2, UJJ0, UPS0, VAL0, VIC0, VNA0, VOS1, VSK0, VSK1, VSS0, WHN0, WIC0, WIK0, WNG0, YAK1, YKC2.

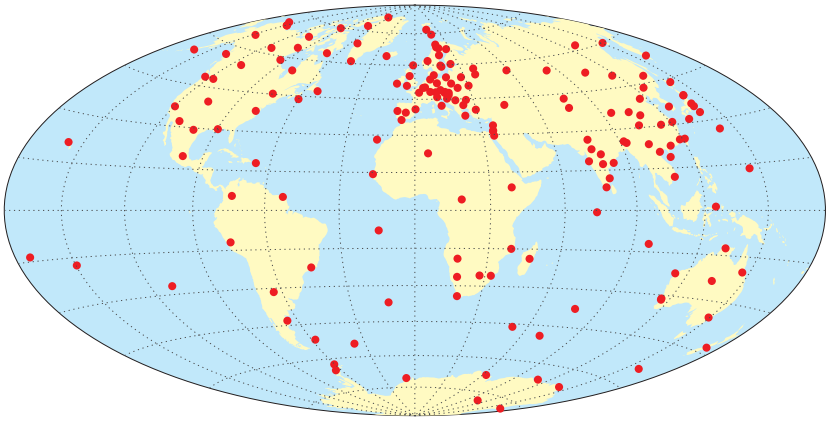

Figure 2: Map showing positions of ground observatories used in the CHAOS-7 field model.

3 Model parameterization

The basic parametrization of the CHAOS-7 field model follows that of previous versions in the CHAOS series, with some minor extension which we describe below. We assume measurements take place in a region free from electric currents, so the vector magnetic field $\mathbf{B}$ may be described by a potential such that $\mathbf{B} = -\nabla V$. The magnetic scalar potential $V = V^{\text{int}} + V^{\text{ext}}$ consists of internal (core and lithospheric) sources, and external (assumed here to be magnetospheric) sources and their internal Earth-induced counterparts. Both internal and external parts are expanded in spherical harmonics. For the internal field, in a geographic Earth-Centered Earth-Fixed (ECEF) coordinate system we adopt a spherical harmonic expansion

$$V^{\text{int}} = a \sum_{n=1}^{N_{\text{int}}} \sum_{m=0}^{n} \left(g_n^m \cos m\phi + h_n^m \sin m\phi \right) \left(\frac{a}{r} \right)^{n+1} P_n^m \left(\cos \theta \right) \qquad (1)$$

where $a = 6371.2$ km is chosen as the spherical reference radius, (r, θ, ϕ) are geographic coordinates, P_n^m are the Schmidt semi-normalized associated Legendre functions, $\{g_n^m, h_n^m\}$ are the Gauss coefficients describing internal sources, and N_{int} is the maximum degree and order of the internal expansion. The internal coefficients $\{g_n^m(t), h_n^m(t)\}$ up to $n = 20$ are time-dependent; this dependence is described by order 6 B-splines [De Boor, 2001] with a 6-month knot separation and five-fold knots at the endpoints $t = 1997.1$ and $t = 2020.1$. Internal coefficients for degrees 21 and above are static, a maximum degree of $N_{int} = 70$ was used for the model described here.

Turning to the external part of the potential, we adopt an expansion in the *Solar Magnetic (SM)* coordinate system (up to $n = 2$, with specific treatment of the $n = 1$ terms, see below) of the near magnetospheric sources and *Geocentric Solar Magnetospheric (GSM)* coordinates (also up to $n = 2$, but restricted to order $m = 0$) of remote magnetospheric sources , e.g., magnetotail and magnetopause currents :

$$\begin{aligned} V^{\text{ext}} = & a \sum_{m=0}^{1} \left(q_1^{m,\text{SM}}(t) \cos mT_d + s_1^{m,\text{SM}}(t) \sin mT_d \right) \left(\frac{r}{a} \right) P_n^m(\cos\theta_d) \\ & + a \sum_{m=0}^{1} \left(\Delta q_1^{m,\text{SM}}(t) R_{1,c}^{m,\text{SM}}(r,\theta,\phi) + \Delta s_1^{m,\text{SM}}(t) R_{1,s}^{m,\text{SM}}(r,\theta,\phi) \right) \\ & + a \sum_{m=0}^{2} \left(q_2^{m,\text{SM}} R_{2,c}^{m,\text{SM}}(r,\theta,\phi) + s_2^{m,\text{SM}} R_{2,s}^{m,\text{SM}}(r,\theta,\phi) \right) \\ & + a \sum_{n=1}^{2} q_n^{0,\text{GSM}} R_n^{0,\text{GSM}}(r,\theta,\phi) \end{aligned} \tag{2}$$

where θ_d and T_d are respectively dipole co-latitude and dipole local time and $R_{n,c/s}^{m,\text{GSM}}$, and $R_{n,c/s}^{m,\text{SM}}$, are modifications of the associated Legendre functions in *SM* and *GSM* coordinate frames taking account of the induced field based on the diagonal part of the Q response matrix for an assumed 3D Earth conductivity model [Olsen, 1999, Grayver et al., 2017]. The degree 1 SM terms have a specific time dependence

$$\begin{aligned} q_1^{0,\text{SM}}(t) &= \hat{q}_1^0 \left[\epsilon(t) + \iota(t) \left(\frac{a}{r} \right)^3 \right] \\ q_1^{1,\text{SM}}(t) &= \hat{q}_1^1 \left[\epsilon(t) + \iota(t) \left(\frac{a}{r} \right)^3 \right] \\ s_1^{1,\text{SM}}(t) &= \hat{s}_1^1 \left[\epsilon(t) + \iota(t) \left(\frac{a}{r} \right)^3 \right] \end{aligned} \tag{3}$$

where the terms in brackets are designed to describe the magnetic field contribution due to the magnetospheric ring-current and its Earth-induced counterpart as estimated by the RC index [Olsen et al., 2014],

$RC(t) = \epsilon(t) + \iota(t)$. The diagonal part of the Q response matrix for an assumed Earth conductivity model [Grayver et al., 2017] was again used for this separation. We estimate static regression factors $\hat{q}_1^0, \hat{q}_1^1, \hat{s}_1^1$ and the time-varying "RC baseline corrections" $\Delta q_1^0, \Delta q_1^1$ and Δs_1^1 in bins of 30 days. These allow for differences between the ground-based estimate of the degree 1 order 0 external magnetic signal (the RC index) and the degree 1 field seen by low-Earth orbit satellites.

In addition to the above spherical harmonic coefficients, we co-estimate Euler angles describing the rotation between the vector magnetometer frame and the star tracker frame for Ørsted, CHAMP, Cryosat-2 and the three Swarm satellites. For Ørsted this yields two sets of Euler angles (one for the period before 24 January 2000 when the onboard software of the star tracker was updated and one for the period after that date), while for CHAMP, Cryosat-2 and each *Swarm* satellite we solve for Euler angles in bins of 10 days.

In order to use the uncalibrated Cryosat-2 data we co-estimate 9 standard calibration parameters (3 scale factors, 3 non-orthogonalities and 3 offsets) in a series of bins of length 31 days. In each bin, these parameters relate the measured vector field in engineering units $\mathbf{E}$ to the calibrated magnetic field $\mathbf{B}$ in units of nanoTesla as follows

$$\mathbf{B} = \underline{\underline{\mathbf{P}}}^{-1} \underline{\underline{\mathbf{S}}}^{-1} (\mathbf{E} - \mathbf{b}), \tag{4}$$

where the matrix describing the non-orthogonalities is

$$\underline{\underline{\mathbf{P}}} = \begin{pmatrix} 1 & 0 & 0 \\ -\sin u_1 & \cos u_1 & 0 \\ \sin u_2 & \sin u_3 & \sqrt{1 - \sin^2 u_2 - \sin^2 u_3} \end{pmatrix}, \tag{5}$$

that describing the scale factors for the fluxgates in the three directions is

$$\underline{\underline{\mathbf{S}}} = \begin{pmatrix} S_1 & 0 & 0 \\ 0 & S_2 & 0 \\ 0 & 0 & S_3 \end{pmatrix}, \tag{6}$$

while the vector containing the offsets is

$$\mathbf{b} = \begin{pmatrix} b_1 \\ b_2 \\ b_3 \end{pmatrix}. \tag{7}$$

Details of the chosen spherical harmonic truncation levels and of temporal parameterization of the various parts of the model are summarized in table 1. In all the model consists of 31757 parameters that are simultaneously estimated from 4007404 magnetic field observations.

Table 1: Summary of parameters defining the model setup in CHAOS-7.

Setup Parameter	Description	
N_{tdep}	Maximum SH degree of time-dependent internal field	20
J	Order of B-Splines	6
Δt_k	B-spline knot spacing	0.5 yr
t_{start}	Start time of spline basis	1997.1
t_{end}	End time of spline	2020.1
N_{int}	Maximum SH degree of static internal field	70
N_{SM}	Maximum SH degree of SM external field	2
ΔT_{SM1}	Bin size for degree 1 SM offsets	30 days
N_{GSM}	Maximum SH degree of SM external field	2 (only $m = 0$ for deg 2)
ΔT_{Euler}	Bin size for Euler and angle determination	10 days
ΔT_{CAL}	Bin size for calibration parameters	31 days

4 Model estimation and regularization

The model parameters $\mathbf{m} = (\mathbf{p}, \mathbf{q}, \mathbf{e})$, where $\mathbf{p}$ represents the spherical harmonic coefficients comprising the field model, $\mathbf{q}$ are the Euler angles and $\mathbf{e}$ is a vector of the calibration parameters, are determined by iteratively minimizing the following cost function using a Newton-type algorithm [Kloss et al., 2019]

$$\Phi(\mathbf{m}) = \big[\mathbf{g}(\mathbf{p}) - \mathbf{d}(\mathbf{q}, \mathbf{e})\big]^{\mathrm{T}} \mathbf{C}_d^{-1} \big[\mathbf{g}(\mathbf{p}) - \mathbf{d}(\mathbf{q}, \mathbf{e})\big] + \mathbf{m}^T \underline{\underline{\Lambda}} \mathbf{m} \tag{8}$$

were $\mathbf{g}(\mathbf{p})$ are model predictions based on field model coefficients, $\mathbf{d}(\mathbf{q}, \mathbf{e})$ are the data, rotated to the geocentric frame using the model Euler angles $\mathbf{q}$ and calibrated (relevant only for Cryosat-2) using the model calibration parameters $\mathbf{e}$. $\mathbf{C}_d$ is a data covariance matrix constructed as in previous versions of the CHAOS model series based on a-prior data error estimates for each satellite, with the vector error estimates specified in the frame of the star tracker which allows the allocation of anisotropic point errors for the Ørsted satellite. Additional data weights proportional to $\sin\theta$ were implemented for the satellite data in order to approximate an equal area distribution. Huber data weights were calculated after each iteration and used to re-weight the data; this enable robust estimation in the presence of long-tailed error distributions. Data error estimates for the ground observatory SV data were derived from residuals to a previous model CHAOS-6x9, after detrending.

In order to calibrate the Cryosat-2 magnetometer data we use data from both sunlit and dark conditions, but only the dark data contributes to the determination of the spherical harmonic coefficients of the field model. A vector calibration is carried out at mid and low latitudes and a scalar calibration at polar latitudes.

Since scalar data are used, and because Euler angles and calibration parameters are co-estimated, the relation between the model parameters and the data is nonlinear. The cost function above was therefore iteratively minimized using a Newton-type descent method, with the Huber data weights updated at each step. The starting model was chosen to be a static internal field from a previous field model CHAOS-6x8 evaluated in May 2015. The external field was initialized to zero. The Euler angles were initialized to the values determined in

pre-flight tests, implemented via a pre-rotation step. The calibration offset and non-orthogonality parameters for Cryosat-2 were initialized to zero, while the scale factors were initialized to values of 1. Nine iterations from this starting model were carried out by which stage we judged that the model had converged to a satisfactory level; the maximum percentage change in a model parameter during the final iteration was 0.1425 %. There was no noticeable change in predictions of the internal field at Earth's surface (i.e. the IGRF relevant part of the model) during the final three iterations.

$\underline{\underline{\Lambda}}$ is a block diagonal temporal regularization matrix which is derived by adding contributing sub-matrices, each of which implements a quadratic measure of the temporal complexity of a certain aspect of the model. These are $\underline{\underline{\Lambda}}_{i3}$, which implements a quadratic measure of the 3rd time derivative of the internal field integrated over the core surface and throughout the model timespan, $\underline{\underline{\Lambda}}_{i2e}$ which implements a quadratic measure of the second time derivative of the internal field integrated over the core surface but only at the model endpoints $t_{start} = 1997.1$ and $t_{end=}2020.1$, $\underline{\underline{\Lambda}}_{sm}$ which implements a quadratic measure of the time derivative (approximated by bin-to-bin differences) of the offset terms in the SM expansion of the magnetospheric field at Earth's surface integrated throughout the timespan, and $\underline{\underline{\Lambda}}_{cs}$, $\underline{\underline{\Lambda}}_{cu}$, $\underline{\underline{\Lambda}}_{cb}$ implement quadratic measures of the time derivative of the Cryosat-2 calibration scale factors, non-orthogonalities and offsets respectively, again implemented using bin-to-bin differences. Each of these temporal regularization sub-matrices are scaled by regularization parameters, denoted by λ_{i3}, λ_{i2e}, λ_{sm}, λ_{cs}, λ_{cu}, λ_{cb}.

There is a special treatment for λ_{i3}, which we allow to vary with the spherical harmonic degree and order (n, m). As was already the case in CHAOS-5 and 6, the zonal ($m = 0$) terms are regularized more strongly than the non-zonal terms, in CHAOS-7 $\lambda_{i3}(n, 0) = 10\lambda_{i3}(n, m > 0)$. Test models showed that the large value of λ_{i3} required to ensure stability at low degree resulted in little time dependence of high degree coefficients. In order to relax the temporal regularization at higher degrees a degree dependence of λ_{i3} was also implemented. It takes its large value $\lambda_{i3}(n_{low}, m)$ at low degree, $n_{low} < n_{tpmin}$, then gradually reduces by a factor 5.10^{-3} by degree n_{tpmax}. We set $n_{tpmin} = 4$ and $n_{tmax} = 11$ and implemented the reduction with degree using a Tukey cosine taper,

$$\begin{aligned}
\lambda_{i3}(n,m) &= \lambda_{i3}(n_{low},m) \qquad \text{for } n < n_{tpmin} \\
\lambda_{i,3}(n,m) &= \lambda_{i3}(n_{low},m)\left\{\frac{0.995}{2}\left[1+\cos\pi\left(\frac{n-n_{tpmin}}{(n_{tpmax}-n_{tpmin})}\right)\right]+0.005\right\} \text{ for } n_{tpmin} \le n \le n_{tpmax} \\
\lambda_{i3}(n,m) &= 0.005\lambda_3(n_{low},m) \qquad \text{for } n > n_{tpmax}
\end{aligned} \tag{9}$$

Table 2: Choice of regularization parameters in CHAOS-7.

Regularization Parameter	Value
$\lambda_{i3}(n_{low}, m > 0)$	1 (nT days^{-3})$^{-2}$
$\lambda_{i3}(n_{low}, m = 0)$	10 (nT days^{-3})$^{-2}$
$\lambda_{i3}(n_{high}, m > 0)$	0.005 (nT days^{-3})$^{-2}$
$\lambda_{i3}(n_{high}, m = 0)$	0.05 (nT days^{-3})$^{-2}$
λ_{i2e}	100 (nT days^{-2})$^{-2}$
λ_{sm}	900 000 (nT days^{-1})$^{-2}$
λ_{cs}	961 ((eu/nT) days^{-1})$^{-2}$
λ_{cu}	9610 (arcsec days^{-1})$^{-2}$
λ_{co}	9.61 (eu days^{-1})$^{-2}$

5 Results for parent model CHAOS-7

5.1 Fit to satellite data

Table 3: Model statistics of misfit between CHAOS-7 and Ørsted data. Mean and rms refer to Huber weighted mean and rms values in units of nT. δF_{NS} denotes along-track field differences calculated at 15 sec spacing.

	Ørsted		
	N	mean	rms
F_{polar}	134139	0.92	3.02
$F_{\mathrm{non-polar}}$	261614	0.53	1.93
B_r	47841	0.01	4.04
B_θ	47841	-0.07	4.73
B_ϕ	47841	0.05	4.80
$\delta F_{\mathrm{NS,polar}}$	68097	-0.00	0.35
$\delta F_{\mathrm{NS,non-polar}}$	142801	0.00	0.19

Table 4: Model statistics of misfit between CHAOS-7 and SAC-C data. Mean and rms refer to Huber weighted mean and rms values in units of nT.

	SAC-C		
	N	mean	rms
F_{polar}	26711	0.10	3.49
$F_{\mathrm{non-polar}}$	48804	0.18	2.43

Table 5: Model statistics of misfit between CHAOS-7 and CHAMP data. Mean and rms refer to Huber weighted mean and rms values in units of nT. δF_{NS} and δB_{NS} denote along-track field differences calculated at 15 sec spacing.

	CHAMP		
	N	mean	rms
F_{polar}	127529	-0.86	4.26
$F_{\mathrm{non-polar}}$	223744	-0.53	1.85
B_r	223744	0.05	1.80
B_θ	223744	0.29	2.48
B_ϕ	223744	0.04	2.08
$\delta F_{\mathrm{NS,polar}}$	77693	0.00	0.75
$\delta F_{\mathrm{NS,non-polar}}$	154347	0.00	0.26
$\delta B_{r,\mathrm{NS}}$	111546	-0.00	0.38
$\delta B_{\theta,\mathrm{NS}}$	111546	-0.01	0.38
$\delta B_{\phi,\mathrm{NS}}$	111546	-0.00	0.40

Table 6: Model statistics of misfit between CHAOS-7 and Cryosat-2 data. Mean and rms refer to Huber weighted mean and rms values in units of nT. Only the misfit to data from dark regions used to determine the field model coefficients is reported here.

	Cryosat-2		
	N	mean	rms
F_{polar}	16761	0.17	5.98
$F_{\mathrm{non-polar}}$	31322	0.02	4.21
B_r	31322	0.08	4.08
B_θ	31322	-0.07	5.23
B_ϕ	31322	-0.22	4.08

Table 7: Model statistics of misfit between CHAOS-7 and *Swarm* data. Mean and rms refer to Huber weighted mean and rms values in units of nT. δF_{NS} and δB_{NS} denote along-track field differences calculated at 15 sec spacing. δF_{EW} and δB_{EW} denote EW field differences between *Swarm* Alpha and Charlie.

	SW-A			SW-B			SW-C			SW-A – SW-C		
	N	mean	rms	N	mean	rms	N	mean	rms	N	mean	rms
F_{polar}	23636	-0.06	3.61	23128	0.05	3.39	23863	0.07	3.59			
$F_{\mathrm{non-polar}}$	44992	-0.07	1.81	46652	-0.07	1.84	45531	0.00	1.80			
B_r	44992	-0.04	1.52	46652	-0.07	1.49	45531	-0.04	1.54			
B_θ	44992	0.09	2.38	46652	0.07	2.44	45531	0.01	2.37			
B_ϕ	44992	0.00	1.91	46652	-0.02	1.98	45531	-0.02	1.94			
$\delta F_{\mathrm{NS,polar}}$	15600	0.01	0.57	15456	0.00	0.51	15735	0.00	0.58			
$\delta F_{\mathrm{NS,non-polar}}$	30570	-0.00	0.14	31658	-0.00	0.12	30599	-0.00	0.14			
$\delta B_{r,\mathrm{NS}}$	22469	-0.00	0.23	23178	0.00	0.22	22958	-0.00	0.24			
$\delta B_{\theta,\mathrm{NS}}$	22469	-0.00	0.24	23178	-0.00	0.23	22958	0.00	0.25			
$\delta B_{\phi,\mathrm{NS}}$	22469	0.00	0.31	23178	0.00	0.30	22958	-0.00	0.32			
$\delta F_{\mathrm{EW,polar}}$										28738	-0.14	0.57
$\delta F_{\mathrm{EW,non-polar}}$										55954	-0.08	0.35
$\delta B_{r,\mathrm{EW}}$										40617	-0.00	0.40
$\delta B_{\theta,\mathrm{EW}}$										40617	-0.00	0.46
$\delta B_{\phi,\mathrm{EW}}$										40617	0.00	0.53

5.2 Fit to observatory data

Table 8: Model statistics of fit of CHAOS-7 to ground observatory (annual differences of revised-monthly mean) data. Mean and rms refer to Huber weighted mean and rms values in units of nT/yr considering observatories from all latitudes.

	Ground observatories		
	N	mean	rms
dB_r/dt	30448	0.11	3.73
dB_θ/dt	30448	-0.21	3.59
dB_ϕ/dt	30448	0.01	3.31

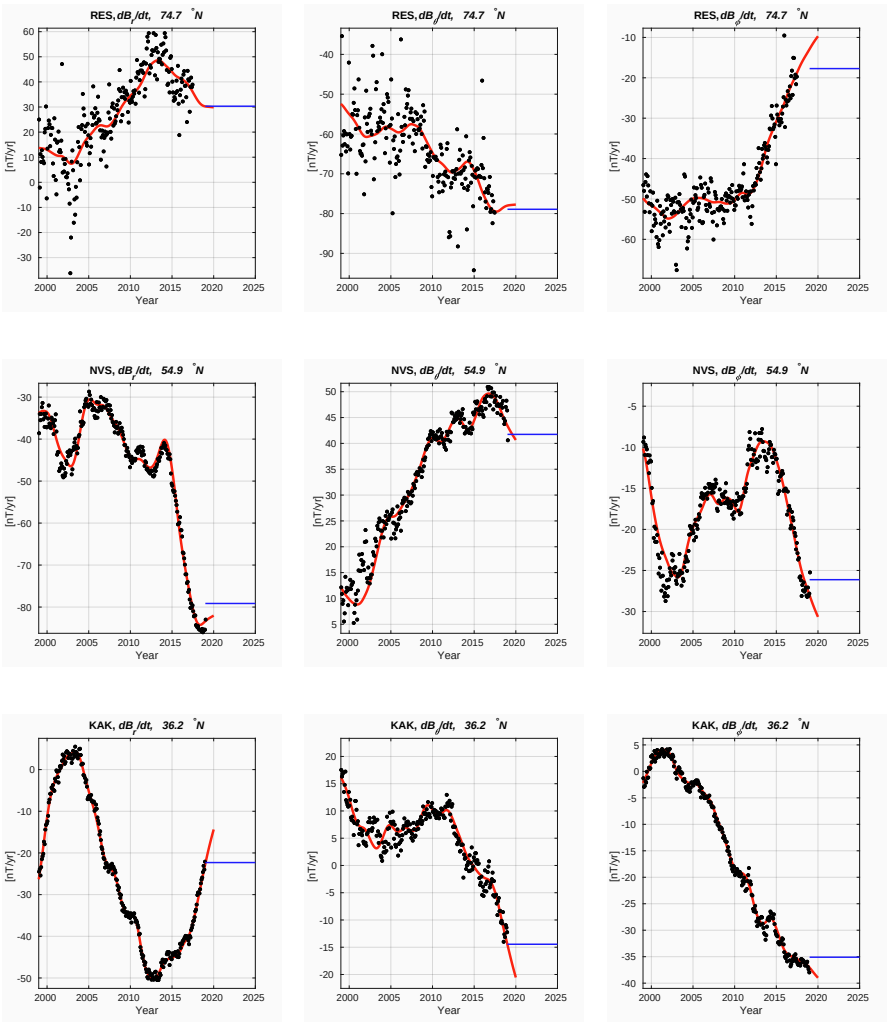

Figure 3: Fit of CHAOS-7 (in red) to secular variation (annual differences of revised monthly means, in black) at example ground observatories. The blue line shows the DTU SV-2020-2025 candidate model.

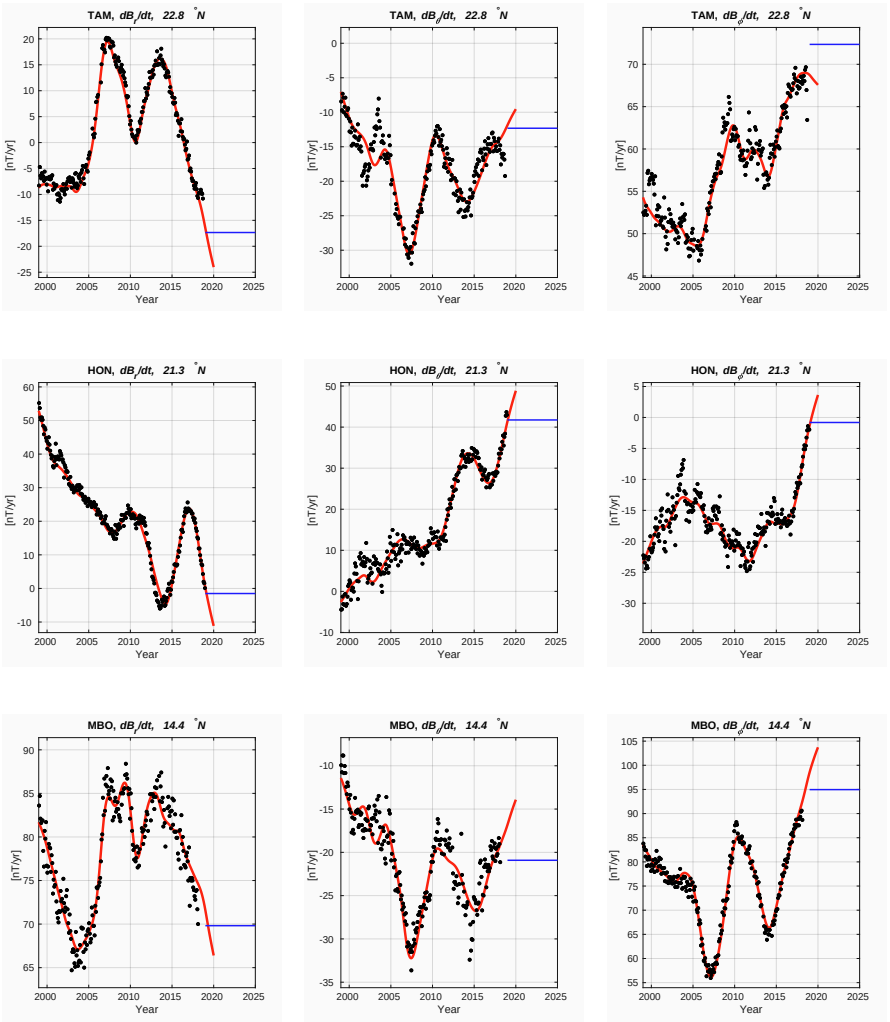

Figure 3: cont.

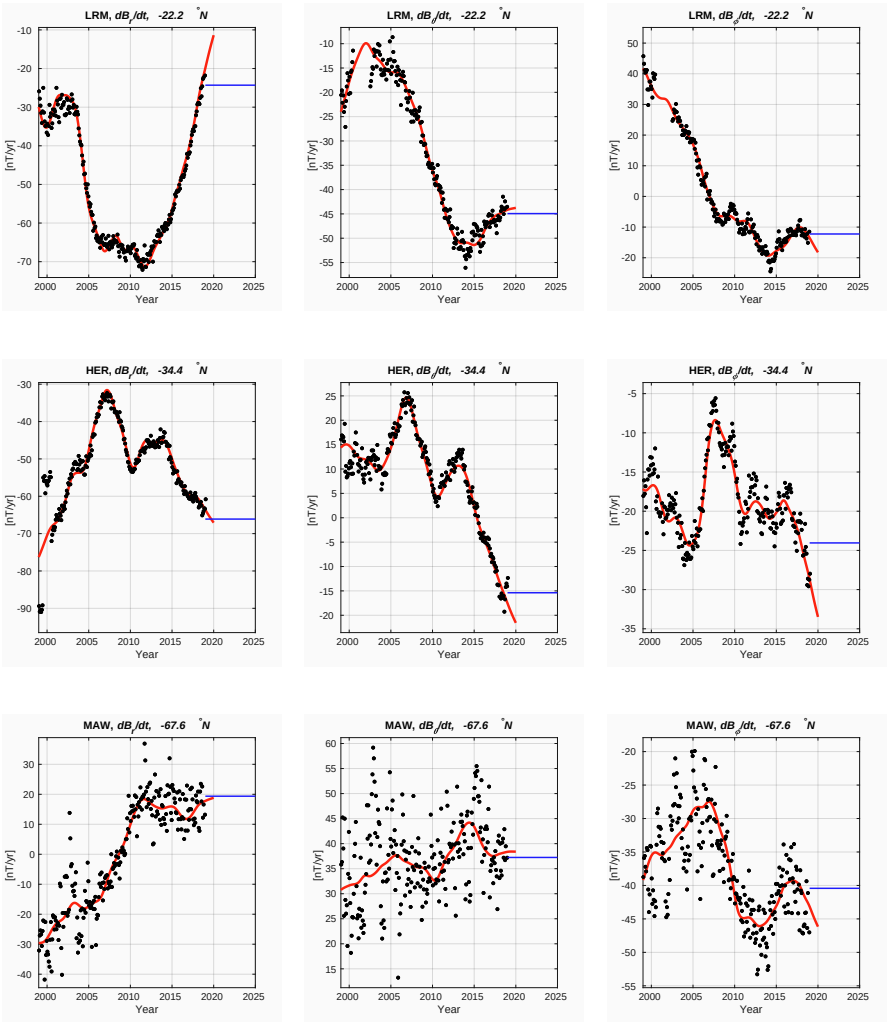

Figure 3: cont.

5.3 Time-dependence of SV coefficients

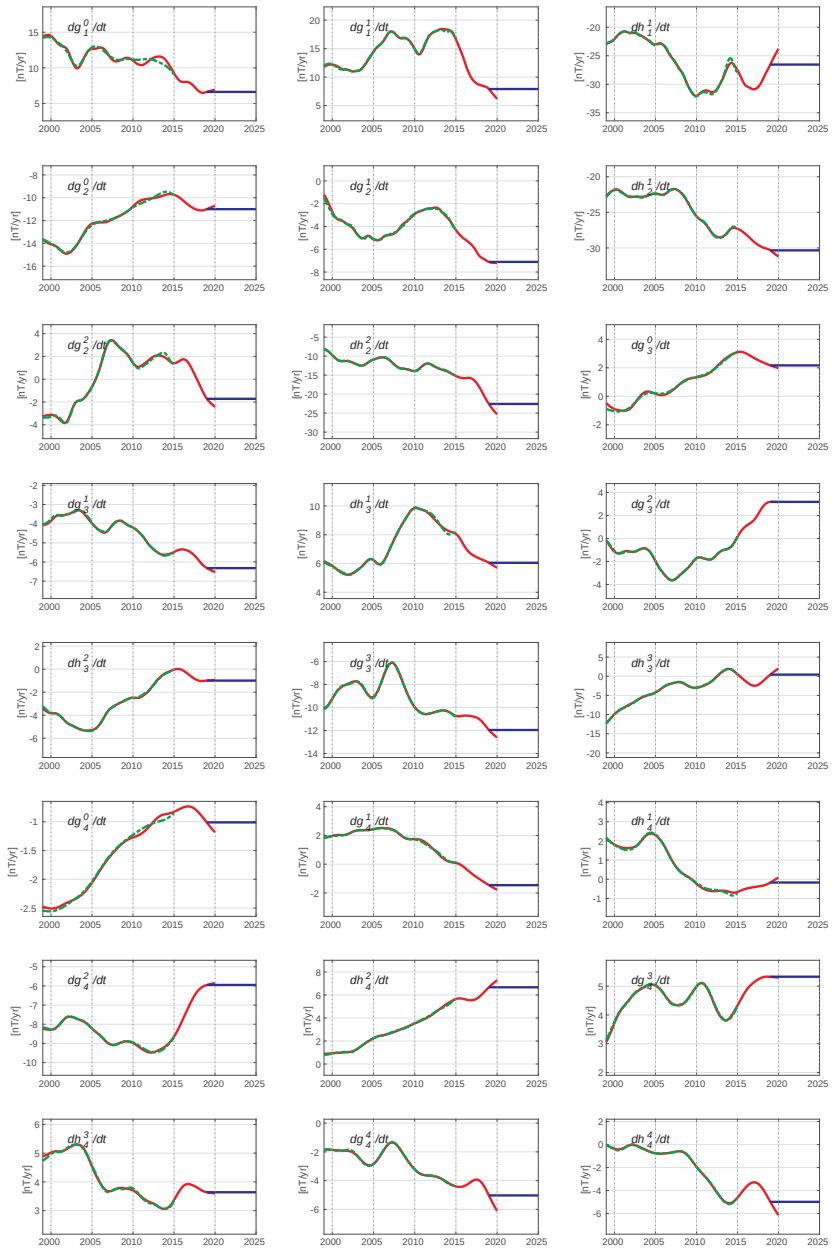

Figure 4: Time-dependence of SH coefficients of the secular variation from CHAOS-7 (solid red line) with CHAOS-6x9 (green dashed line) also shown for reference. The blue line shows the DTU SV-2020-2025 candidate model.

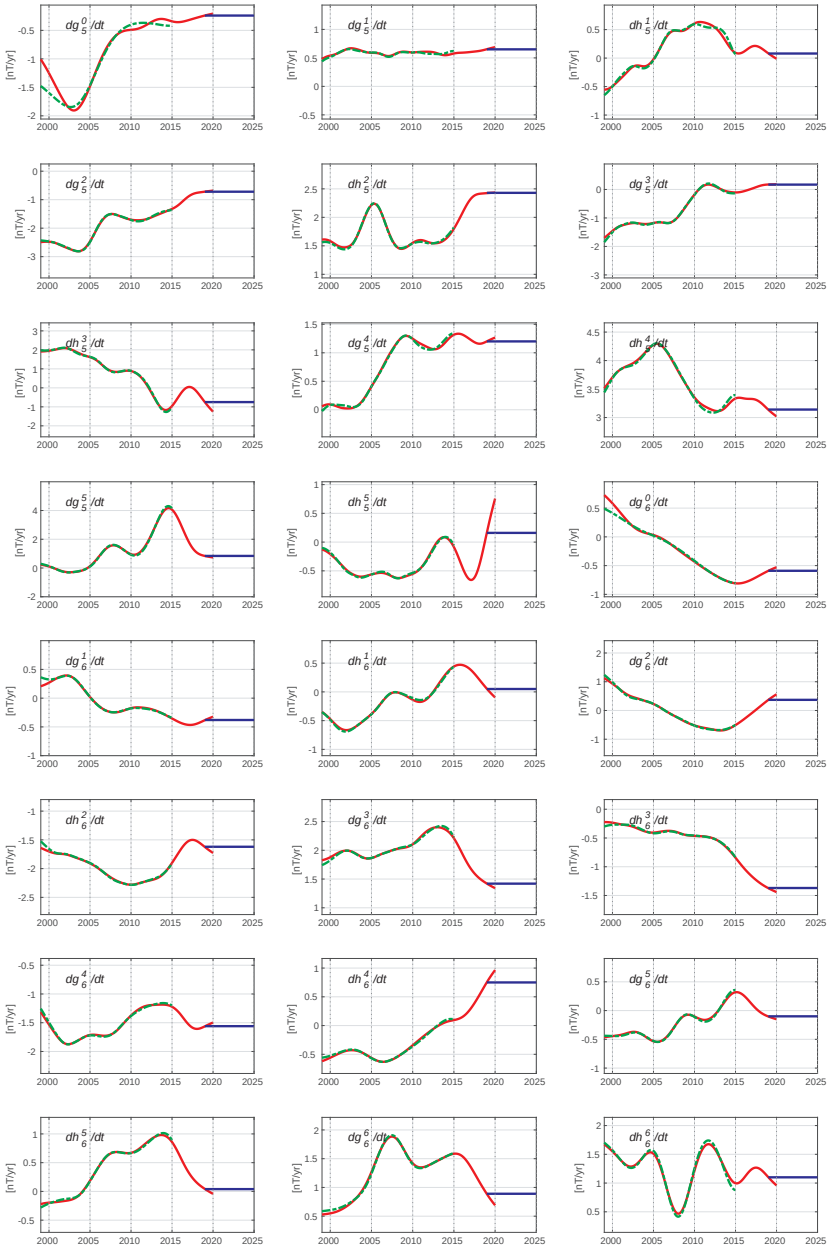

Figure 4: cont.

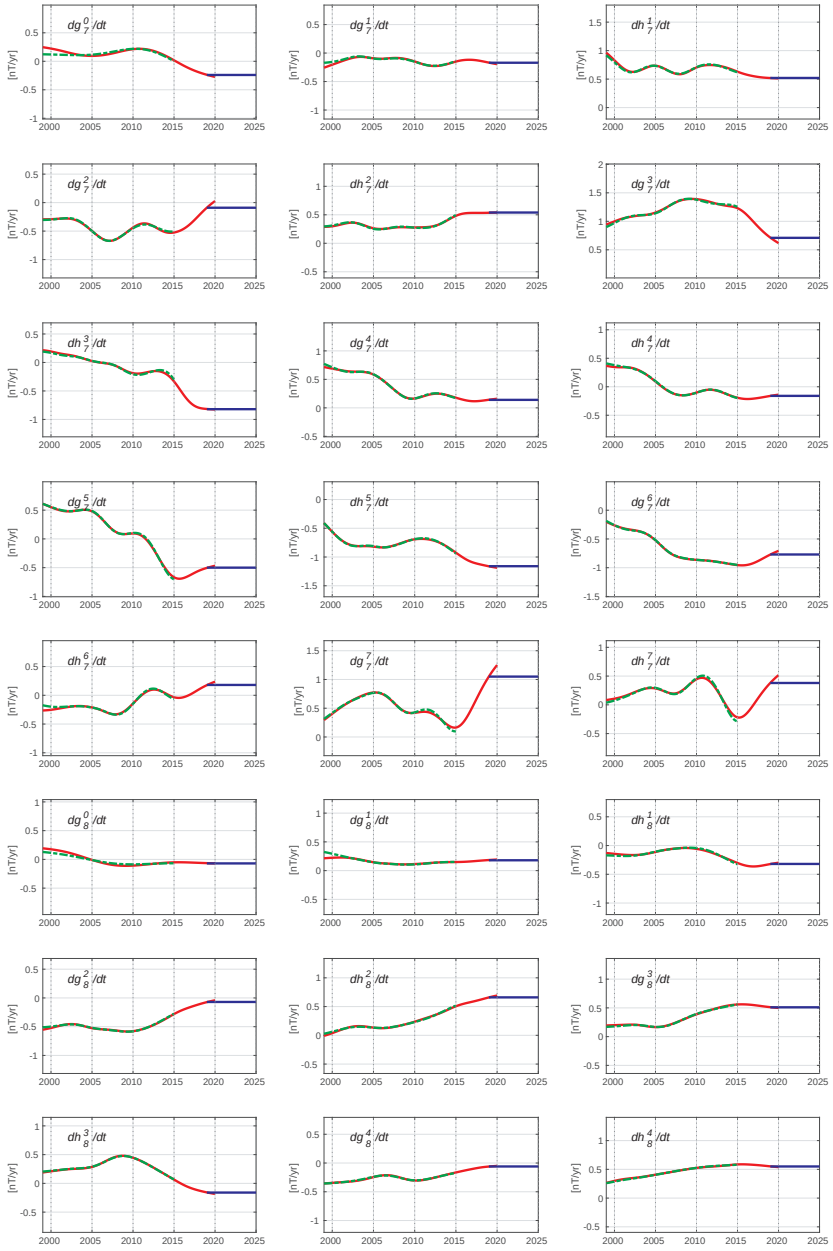

Figure 4: cont.

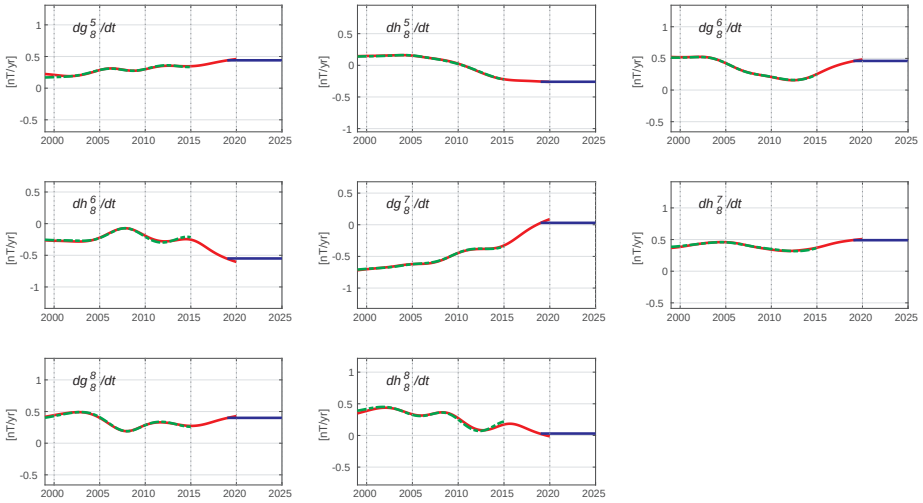

Figure 4: cont.

5.4 Spherical harmonic power spectra

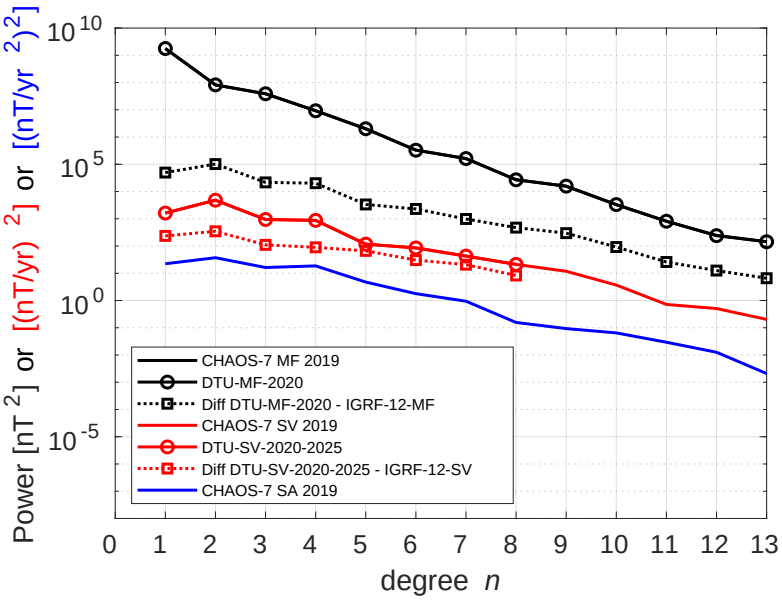

Figure 5: Spherical harmonic spectra at the Earth's surface. Mean square vector magnetic field (black solid line), its first derivative (SV, red solid line), its and second derivative (SA, blue solid line) from CHAOS-7 in epoch 2019.0. The DTU candidate models for IGRF MF in 2020 is marked by the black circles, and the DTU SV-2020-2025 candidate is marked by the red circles. Differences between these candidates and the previous IGRF-12 MF and SV models are shown by the dashed lines with black squares and red squares respectively.

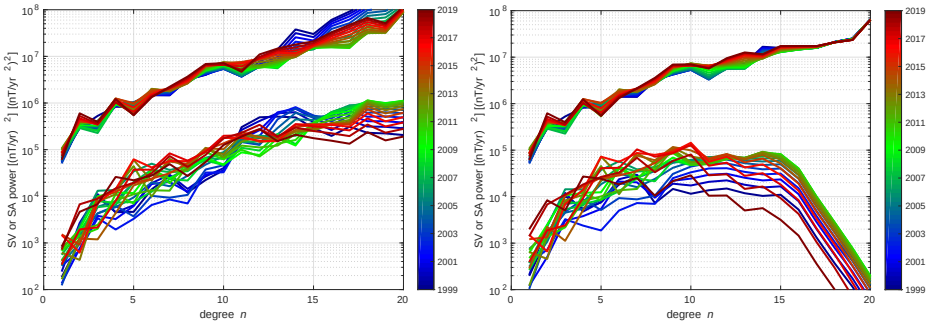

Figure 6: Spherical harmonic spectra of the mean square SV and SA at the Earth's core from CHAOS-7, colours show different epochs. Left is for CHAOS-7, right shows for reference CHAOS6-x9.

5.5 Co-estimated calibration parameters for Cryosat-2

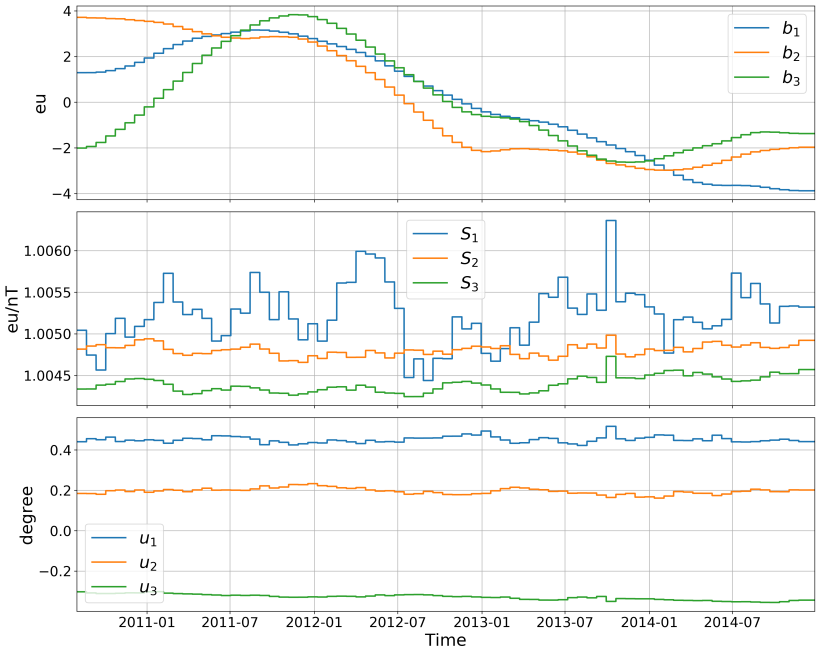

Figure 7: Time variation of co-estimated calibration parameters for Cryosat-2 FGM-1. Top shows the offsets, middle shows the scale factors and bottom the non-orthogonalities

6 Extraction of IGRF candidate models

IGRF-13 candidates were extracted from the parent model CHAOS-7 as follows:

- **DGRF, epoch 2015.0**
  The parent model CHAOS-7, with its spline-based time-dependence, was evaluated at epoch 2015.0 and the internal spherical harmonic coefficients up to degree and order 13 output to 0.01 nT.

- **IGRF, epoch 2020.0**
  The parent model CHAOS-7, with its spline-based time-dependence was evaluated at epoch 2019.75 when the last input satellite data were available to constrain the model. The resulting coefficients were then propagated forward to epoch 2020.0, using the linear SV evaluated from CHAOS-7 in epoch 2019.0 (as in our SV candidate described below, to avoid spline-model end effects and to take advantage of the latest available SV constraints from annual differences of ground observatory monthly means), for all spherical harmonics up to degree 13, as follows:

$$g_n^m(t = 2020.0) = g_n^m(t = 2019.75) + 0.25 \cdot \dot{g}_n^m(t = 2019.0) \qquad (10)$$

  Here g_n^m represents each of the Gauss coefficients $\{g_n^m, h_n^m\}$ while $\dot{g}_n^m$ represents the SV coefficients $\{\dot{g}_n^m, \dot{h}_n^m\}$ in nT/yr. The resulting spherical harmonic coefficients for the internal field in epoch 2020.0 up to degree and order 13 were output to 0.01 nT.

- **Predicted average SV, 2020.0 to 2025.0**
  Since there can be spline-model end effects in the secular acceleration (SA), we evaluated the SV from CHAOS-7 at epoch 2019.0, rather than in 2020.0, and did not attempt any extrapolation. These end effects are essentially due to the lack of 'future' data for constraining the SV and SA at the model endpoint, and because SV estimates based on annual differences of ground observatory monthly means are available only up to 6 months before the latest available ground observatory data. Recall that the SV in a spline-based model such as CHAOS-7 at a particular epoch is not the true instantaneous SV, but a weighted time-average, with the amount of time-averaging varying with spherical harmonic degree according to the imposed regularization.

  The SV spherical harmonic coefficients (first time derivative of the spline model) for the internal field in epoch 2019.0, up to degree and order 8 were then output to 0.01 nT/yr. We provide also SV predictions to degree and order 13 as a test secular variation model.

No uncertainty estimates were provided with our candidate models, since we are unable to calculate satisfactory estimates. The largest errors are likely biases caused by unmodelled sources (e.g. the highy dynamic polar electrojet) which cannot be assessed using a formal model error covariance matrix, or by constructing models using the same technique from independent datasets.

7 Summary

We have presented the CHAOS-7 geomagnetic field model which is the basis for DTU's IGRF-13 candidate models. We find CHAOS-7 represents well data from seven satellites over the past 20 years, and captures well the trends in secular variation as observed at ground observatories. Our DGRF 2015 candidate is based directly on values of the internal field from CHAOS-7 in 2015, at an epoch where good data constraints were available from the *Swarm* satellites. Our IGRF 2020 candidate model is based on the internal field from CHAOS-7 in 2019.75 (at the time of the last contributing data) propagated to 2020 using the secular variation from CHAOS-7 in 2019.0 /when the last constraints from annual differences of ground data were available). The latter also supplies our predictive SV models for the period 2020 to 2025 since we know of no reliable way to forecast future SV changes.

Acknowledgements

We wish to thank ESA for the prompt availability of *Swarm* L1b data and for providing access to the Cryosat-2 platform magnetometer data and related engineering information. The support of the CHAMP mission by the German Aerospace Center (DLR) and the Federal Ministry of Education and Research is gratefully acknowledged. The Ørsted Project was made possible by extensive support from the Danish Government, NASA, ESA, CNES, DARA and the Thomas B. Thriges Foundation. The staff of the geomagnetic observatories and INTERMAGNET are thanked for supplying high-quality observatory data. Susan Macmillan (BGS) is gratefully acknowledged for collating checked and corrected observatory hourly mean values in the AUX_OBS database. Alexander Grayver is thanked for providing the Q matrix and convolution kernels for the conductivity model of Grayver et al., (2017).

References

De Boor, C. (2001). A practical guide to splines. *Applied Mathematical Sciences*, 27.

Finlay, C. C., Olsen, N., Kotsiaros, S., Gillet, N., and Toeffner-Clausen, L. (2016). Recent geomagnetic secular variation from *Swarm* and ground obser-

vatories as estimated in the CHAOS-6 geomagnetic field model. *Earth Planets Space*, 68(1):1–18.

Friis-Christensen, E., Finlay, C. C., Hesse, M., and Laundal, K. M. (2017). Magnetic field perturbations from currents in the dark polar regions during quiet geomagnetic conditions. *Space Science Reviews*, 206(1):281–297.

Grayver, A. V., Munch, F. D., Kuvshinov, A. V., Khan, A., Sabaka, T. J., and Tøffner-Clausen, L. (2017). Joint inversion of satellite-detected tidal and magnetospheric signals constrains electrical conductivity and water content of the upper mantle and transition zone. *Geophysical Research Letters*, 44(12):6074–6081.

Huber, P. J. (2004). *Robust statistics*. Wiley.

Kloss, C., Olsen, N., and Finlay, C. C. (2019). Extending geomagnetic field modeling to include co-estimation of calibration parameters of vector field data. *Earth, Planets and Space*, in prep.

Macmillan, S. and Olsen, N. (2013). Observatory data and the Swarm mission. *Earth, Planets and Space*, 65:1355–1362.

Olsen, N. (1999). Induction studies with satellite data. *Surveys in Geophysics*, 20:309–340.

Olsen, N., Kloss, C., and Tøffner-Clausen, L. (2019). Calibration of Cryosat-2 platform magnetometer data. *Earth, Planets and Space*, in prep.

Olsen, N., Lühr, H., Finlay, C. C., and Tøffner-Clausen, L. (2014). The CHAOS-4 Geomagnetic Field Model. *Geophys. J. Int.*, 1997:815–827.

Olsen, N., Lühr, H., Sabaka, T. J., Mandea, M., Rother, M., Tøffner-Clausen, L., and Choi, S. (2006). CHAOS – a model of Earth's magnetic field derived from CHAMP, Ørsted, and SAC-C magnetic satellite data. *Geophys. J. Int.*, 166:67–75.

Sabaka, T. J., Olsen, N., and Purucker, M. E. (2004). Extending comprehensive models of the Earth's magnetic field with Ørsted and CHAMP data. *Geophys. J. Int.*, 159:521–547.